Physical mechanism of the electron-ion coupled transverse instability in laser pressure ion acceleration for different regimes

Y. Wan,[1,2,*] C.-H. Pai,[1] C. J. Zhang,[3] F. Li,[3] Y. P. Wu,[1] J. F. Hua,[1] W. Lu,[1,†] C. Joshi,[3] W. B. Mori,[3] and V. Malka[2,4]

[1]*Department of Engineering Physics, Tsinghua University, Beijing 100084, China*

[2]*Department of Physics of Complex Systems, Weizmann Institute of Science, Rehovot 7610001, Israel*

[3]*University of California–Los Angeles, Los Angeles, California 90095, USA*

[4]*Laboratoire d'Optique Appliquée, ENSTA-CNRS-Ecole Polytechnique, UMR7639, 91761 Palaiseau, France*

(Received 22 March 2018; revised manuscript received 7 June 2018; published 11 July 2018)

In radiation pressure ion acceleration (RPA) research, the transverse stability within laser plasma interaction has been a long-standing, crucial problem over the past decades. In this paper, we present a one-dimensional two-fluid theory extended from a recent work Wan *et al.* Phys. Rev. Lett. **117**, 234801 (2016) to clearly clarify the origin of the intrinsic transverse instability in the RPA process. It is demonstrated that the purely growing density fluctuations are more likely induced due to the strong coupling between the fast oscillating electrons and quasistatic ions via the ponderomotive force with spatial variations. The theory contains a full analysis of both electrostatic (ES) and electromagnetic modes and confirms that the ES mode actually dominates the whole RPA process at the early linear stage. By using this theory one can predict the mode structure and growth rate of the transverse instability in terms of a wide range of laser plasma parameters. Two-dimensional particle-in-cell simulations are systematically carried out to verify the theory and formulas in different regimes, and good agreements have been obtained, indicating that the electron-ion coupled instability is the major factor that contributes the transverse breakup of the target in RPA process.

DOI: 10.1103/PhysRevE.98.013202

I. INTRODUCTION

Ion acceleration driven by ultraintense lasers has become a very active topic since the experimental observation of an intense proton beam with the maximum energy of 58 MeV in 2000 [1–3]. Energetic ion sources from compact laser plasma-based acceleration have many unique features such as ultrashort pulse duration, micron-scale size, and ultrahigh peak current compared with those from conventional radio-frequency accelerators, and thus have great potential for many applications, including ultrafast radiography [4–6], cancer therapy [7,8], fast ignition [9–11], etc.

Among all the existing acceleration mechanisms, radiation pressure ion acceleration (RPA) has attracted much attention worldwide for its properties of monoenergetic acceleration with high-energy conversion efficiency in one-dimensional (1D) geometry [12–17]. The concept of RPA was first proposed by Esirkepov *et al.* [12] in 2004. Their three-dimensional (3D) particle-in-cell (PIC) simulations showed that GeV quasi-monoenergetic ion beams can be obtained by employing a superintense linearly polarized laser (10^{23} W/cm^2) to interact with a thin foil. Soon afterwards, Macchi *et al.* [13] through 1D PIC simulations found that circularly polarized (CP) lasers with moderate intensity can provide a prominent radiation pressure effect, as the nonoscillating ponderomotive force in this case applies a steady pressure to the target front and forms a quasistatic high-density layer moving forward. This is known as the hole boring (HB) process [13,18]. Similarly, for a ultrathin foil, the compressed electron and ion layers can be pushed and accelerated as a whole by the laser pressure in the so-called light sail process [12,14–17,19,20] and monoenergetic ion beams can be generated.

Though radiation pressure ion acceleration (RPA) seems very attractive in ideal 1D geometry, it is still quite challenging for its experimental realization. Until now, the experimental progress on RPA has been very limited [21–24]. Objectively, there are two aspects of reasons that can be applied for the explanation of RPA's current status: on one hand, it is very demanding on the laser contrast and the manufacture of a nano-foil target, which is still hard to achieve in the present experiments [2,3]; on the other hand, key physical effects like laser pressure nonuniformity-induced electron heating [15–17] and transverse instability [15,16,25–31] can significantly affect the physical process in multidimensional geometry. In reality, the RPA scheme has been suffering from the transverse instability since it was proposed. Previous two-dimensional (2D) and 3D simulations showed that for either thick or thin foils, there are always transverse density ripples induced at the front surface irradiated by the laser pulse, which can grow very significantly, breaking up the target and prematurely terminating the RPA process [15,16,26–31]. This phenomenon even shows up for a laser with a transversely uniform profile [15,25,32]. Over the past decades, many mechanisms have been proposed to try to explain the formation of these transverse ripples, such as Rayleigh-Taylor-like instability [16,25,32–35], Weibel-like instability [28,29,36–39], and so on. Among them, for linearly polarized lasers [36–39], Weibel-related instabilities from strong electron heating seem to be major factors that contribute

*yang.wan@weizmann.ac.il

†weilu@tsinghua.edu.cn

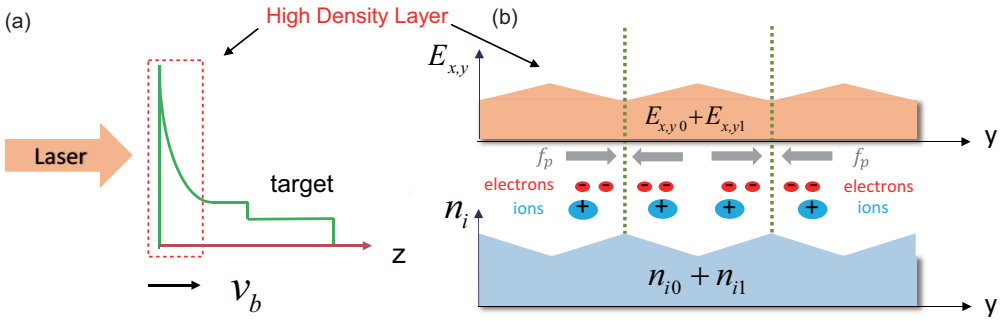

FIG. 1. (a) The schematic model of the hole boring process by radiation pressure. (b) The physical picture of transverse instability within the high-density layer. z represents the longitudinal direction and x and y represent the transverse directions. n_{i1} and $E_{x,y1}$ represent the ion density and the transverse electric field fluctuations, respectively. f_p represents the ponderomotive force.

to the surface ripples. However, for circularly polarized lasers (mainly used for RPA), none of these models are able to give accurate predictions of the mode structure and its growth rate consistent with PIC simulations for a wide range of laser plasma parameters.

In this article, we will present a predictive theoretical model extended from a recent work [40] to analyze in detail the transverse instability in the RPA process. It turns out that the transverse density fluctuations are mainly due to the strong coupling between the fast oscillating electrons and quasistatic ions via the induced transverse ponderomotive force with spatial variations. The physical picture of this process is illustrated in Fig. 1. In the longitudinal direction, as shown in Fig. 1(a), a high-density layer is formed and pushed forward stably by the laser pressure after a equilibrium between the electrostatic force and laser pressure is built. In the transverse direction of the high-density layer [see Fig. 1(b)], the penetrating CP laser fields oscillate at the laser frequency. If there is a small ion density fluctuation, it can easily couple with the oscillating laser field to excite a fluctuation of electron oscillation, which can then beat with the laser field to generate spacial variations along the transverse direction, giving rise to a ponderomotive force. This force of stationary parts can in turn drive electrons to enhance the ion density fluctuations. After several feedback loops, the transverse instability can finally result. It is noted that this process is similar to the oscillating two-stream instability in inertial confinement fusion research [41,42]. However, significant distinctions exists: first, the laser field penetrates only within the compressed high-density layer formed by the laser pressure, with its amplitude determined by the boundary conditions at the front surface; second, for RPA, the adopted laser here is relativistically intense, with the normalized vector potential a_0 on the order of 1, much larger than those studied in the early studies related to oscillating two-stream instability [41,42].

This paper is organized as follows. In Sec. II a basic 1D theory of the transverse instability is carefully derived, which contains a full treatment of both electrostatic and electromagnetic perturbations. In Secs. III and IV, the mode structure and its growth rate in three different regimes [$a_0 < 1$, $a_0 > 1$ for a thick foil (HB) and thin foil (LS)] are derived and systematically verified by 2D PIC simulations. The work is summarized in Sec. V.

II. THEORETICAL MODEL OF THE TRANSVERSE INSTABILITY

In this section, a 1D theoretical model of this instability will be derived based on the above physical picture. In this configuration, a circularly polarized laser normally incidents on the front surface of a target and launches a high-density layer by its radiation pressure. Thus a full set of two-fluid (electron and ion) plasma description can be written as

$$\frac{\partial n_{(i,e)}}{\partial t} + \vec{\nabla}\cdot(n_{(i,e)}\vec{v}_{(i,e)}) = 0, \tag{1a}$$

$$\frac{\partial \vec{P}_{(i,e)}}{\partial t} + \vec{v}_{(i,e)}\cdot\vec{\nabla}(\vec{P}_{(i,e)}) = -q_{(i,e)}\left(\vec{\nabla}\Phi + \frac{1}{c}\frac{\partial \vec{A}}{\partial t}\right) + q_{(i,e)}\frac{v_{(i,e)}}{c}\times\vec{\nabla}\times\vec{A} - \frac{\vec{\nabla}(n_{i,e}T_{i,e})}{n_{i,e}}, \tag{1b}$$

$$\left(\frac{1}{c^2}\frac{\partial^2}{\partial t^2} - \nabla^2\right)\vec{A} = \frac{4\pi}{c}\vec{j} - \vec{\nabla}\left(\frac{1}{c}\frac{\partial \Phi}{\partial t} + \vec{\nabla}\cdot\vec{A}\right), \tag{1c}$$

$$\vec{\nabla}\cdot\left[\vec{\nabla}\Phi + \frac{1}{c}\frac{\partial \vec{A}}{\partial t}\right] = -4\pi(q_i n_i - e n_e), \tag{1d}$$

where $\vec{v}$, $\vec{P}$, q, and T are the particle velocity, momentum, charge, and temperature, respectively; Φ and $\vec{A}$ are the scalar and vector potential; $\vec{j}$ is the beam current density; and c is the light speed in vacuum.

It is known that the ponderomotive force mainly comes from two parts, the $\vec{E}\cdot\vec{\nabla}\vec{E}$ and $\vec{v}\times\vec{B}$, which respectively contribute to the instabilities of electrostatic (ES) mode and electromagnetic (EM) modes. In the following derivation, we define z as the laser propagation (longtudinal) direction and (x,y) as transverse directions, and these two modes will be carefully studied separately.

For simplicity, we adopt the Coulomb gauge $\vec{\nabla}\cdot\vec{A} = 0$, and consider only the fluctuations along one of the transverse (y) directions.

First, the ES mode is analyzed. This mode is stimulated by the P-polarization part of the CP laser through $\vec{E}\cdot\vec{\nabla}\vec{E}$ effect. Here we only adopt $A_{y0} = A_0\sin(\omega_0 t + \phi)$ (P-polarization) as

the initial laser vector potential, where ω_0 is laser frequency, and ϕ is the initial phase.

In the comoving frame of the high-density layer, the two-fluid equations for electrons and ions in the y direction are

$$\frac{\partial n_{(i,e)}}{\partial t}+\frac{\partial n_{(i,e)}v_{(i,e)y}}{\partial y}=0, \tag{2a}$$

$$\frac{\partial P_{(i,e)y}}{\partial t}+v_{(i,e)y}\frac{\partial P_{(i,e)y}}{\partial y} \tag{2b}$$
$$=-q_{(i,e)}\left(\frac{\partial\Phi}{\partial y}+\frac{1}{c}\frac{\partial A_y}{\partial t}\right)-\frac{1}{n_{i,e}}\frac{\partial(n_{i,e}T_{i,e})}{\partial y},$$

$$\left(\frac{\partial^2}{\partial z^2}+\frac{\partial^2}{\partial y^2}\right)\Phi=-4\pi(q_in_i-en_e). \tag{2c}$$

For simplicity, we assume the target is fairly flat and the density fluctuation depends only on (y,t). To linearize the fluid equations, all the quantities can be decomposed as a stationary part plus a first-order quantity, such as $v_{ey}=v_{ey0}+v_{ey1}$, $P_{ey}=P_{ey0}+P_{ey1}$, $v_{iy}=v_{iy0}+v_{iy1}$ $(v_{iy0}=0)$, $n_e=n_{e0}+n_{e1}$, $n_i=n_{i0}+n_{i1}$, $A_y=A_{y0}+A_{y1}$, and $\Phi=\Phi_0+\Phi_1$, where $P_{ey0}=P_{os}\sin(\omega_0t+\phi)$ (based on the conservation of canonical momentum). Here ions are assumed nonrelativistic and $T_i=0$. Based on the Coulomb gauge $\vec{\nabla}\cdot\vec{A}=0$, one can get $A_{y1}=0$.

Then the equations for only first-order quantities can be obtained as

$$\frac{\partial n_{e1}}{\partial t}+v_{ey0}\frac{\partial n_{e1}}{\partial y}+n_{e0}\frac{\partial v_{ey1}}{\partial y}=0, \tag{3a}$$

$$\frac{\partial P_{ey1}}{\partial t}+v_{ey0}\frac{\partial P_{ey1}}{\partial y}=e\frac{\partial\Phi_1}{\partial y}-\frac{1}{n_{e0}}\frac{\partial(n_{e1}T_e)}{\partial y}, \tag{3b}$$

$$\frac{\partial n_{i1}}{\partial t}+n_{e0}\frac{\partial v_{iy1}}{\partial y}=0, \tag{3c}$$

$$\frac{\partial v_{iy1}}{\partial t}=-\frac{q_i}{m_i}\frac{\partial\Phi_1}{\partial y}, \tag{3d}$$

$$\frac{\partial^2\Phi_1}{\partial y^2}=-4\pi(q_in_{i1}-en_{e1}), \tag{3e}$$

where m_i represents the ion rest mass. From Eqs. (3), it is indeed the term $v_{ey0}\frac{\partial P_{ey1}}{\partial y}$, corresponding to $E_{y0}\frac{\partial E_{y1}}{\partial y}$, that triggers the instability. Thus, the P-polarization part of a CP laser stimulates only the ES mode.

By assuming all first-order quantities have the form of $\exp[i(ky-\omega t)]$, one can get the following equations in (ω, k) space:

$$-i\omega n_{e1}(\omega)-\frac{v_{os}k}{2}[n_{e1}(\omega+\omega_0), \tag{4a}$$

$$-n_{e1}(\omega-\omega_0)]+ikn_{e0}v_{ey1}(\omega)=0,$$

$$-i\omega P_{ey1}(\omega)-\frac{v_{os}k}{2}[P_{ey1}(\omega+\omega_0) \tag{4b}$$

$$-P_{ey1}(\omega-\omega_0)]=ike\Phi_1(\omega)-\frac{1}{n_{e0}}ikn_{e1}T_e$$

$$-i\omega n_{i1}(\omega)+ikn_{i0}v_{iy1}(\omega)=0 \tag{4c}$$

$$-i\omega v_{iy1}(\omega)=-\frac{ikq_i\Phi_1(\omega)}{m_i} \tag{4d}$$

$$-k^2\Phi_1(\omega)=-4\pi[q_in_{i1}(\omega)-en_{e1}(\omega)]. \tag{4e}$$

For simplicity, in the following, mass is in units of electron rest mass m_e, velocity in light speed of vacuum c, and charge in electron charge e. After eliminating n_{i1}, $v_{e,iy1}$, and E_{y1}, it is straightforward to obtain

$$-i\omega n_{e1}(\omega)-\frac{v_{os}k}{2}[n_{e1}(\omega+\omega_0)-n_{e1}(\omega-\omega_0)]$$
$$+ikn_{e0}\kappa P_{ey1}(\omega)=0, \tag{5a}$$

$$-i\omega P_{ey1}(\omega)-\frac{v_{os}k}{2}[P_{ey1}(\omega+\omega_0)-P_{ey1}(\omega-\omega_0)]$$
$$-\epsilon(\omega)n_{e1}(\omega)=0, \tag{5b}$$

where $v_{os}=P_{os}/\gamma_0$ is the electron quiver velocity amplitude in the laser electric field, and γ_0 is the electron's zero-order Lorentz factor; $\epsilon(\omega)=i[kT_e/n_{e0}-4\pi\omega^2/k(\omega_{pi}^2-\omega^2)]$, $\kappa=(2-v_{os}^2)/2\gamma_0$; and ω_{pi} is the ion plasma frequency. These two equations show the relationship between n_{e1} and P_{ey1} at ω and $\omega\pm\omega_0$. By replacing ω with $\omega\pm\omega_0$, one can obtain another four equations describing the relationship among ω, $\omega\pm\omega_0$, and $\omega\pm2\omega_0$. Since ions also get involved in the whole process, their dynamics are typically on a much slower timescale than the laser oscillation (i.e., $\omega\ll\omega_0$). In order to obtain a closed dispersion relation, we may drop the $\omega\pm2\omega_0$ components as fast-timescale and off-resonant terms. For ions, we keep only the ω components, and electrons are treated as isothermal in the case of $\omega_{pe}\gg\omega_0$, where ω_{pe} is the electron plasma frequency. The substituted four equations are presented as

$$-i(\omega+\omega_0)n_{e1}(\omega+\omega_0)-\frac{v_{os}k}{2}[-n_{e1}(\omega)]+ikn_{e0}\kappa P_{ey1}(\omega+\omega_0)=0, \tag{6a}$$

$$-i(\omega+\omega_0)P_{ey1}(\omega+\omega_0)-\frac{v_{os}k}{2}[-P_{ey1}(\omega)]+i\left(\frac{4\pi}{k}+\frac{kT_e}{n_{e0}}\right)n_{e1}(\omega+\omega_0)=0, \tag{6b}$$

$$-i(\omega-\omega_0)n_{e1}(\omega-\omega_0)-\frac{v_{os}k}{2}[n_{e1}(\omega)]+ikn_{e0}\kappa P_{ey1}(\omega-\omega_0)=0, \tag{6c}$$

$$-i(\omega-\omega_0)P_{ey1}(\omega-\omega_0)-\frac{v_{os}k}{2}[P_{ey1}(\omega)]+i\left(\frac{4\pi}{k}+\frac{kT_e}{n_{e0}}\right)n_{e1}(\omega-\omega_0)=0. \tag{6d}$$

Therefore, we now have six closed equations for six quantities (n_{e1}, P_{ey1} at ω and $\omega \pm \omega_0$), and this can be cast into a matrix form as follows:

$$\begin{pmatrix} -i\omega & -\frac{v_{os}k}{2} & \frac{v_{os}k}{2} & ikn_{e0}\kappa & 0 & 0 \\ \frac{v_{os}k}{2} & -i(\omega+\omega_0) & 0 & 0 & ikn_{e0}\kappa & 0 \\ -\frac{v_{os}k}{2} & 0 & -i(\omega-\omega_0) & 0 & 0 & ikn_{e0}\kappa \\ i\left[\frac{kT_e}{n_{e0}} - \frac{4\pi\omega^2}{k\left(\omega_{pi}^2-\omega^2\right)}\right] & 0 & 0 & -i\omega & -\frac{v_{os}k}{2} & \frac{v_{os}k}{2} \\ 0 & i\left(\frac{4\pi}{k}+\frac{kT_e}{n_{e0}}\right) & 0 & v_{os}k/2 & -i(\omega+\omega_0) & 0 \\ 0 & 0 & i\left(\frac{4\pi}{k}+\frac{kT_e}{n_{e0}}\right) & -\frac{v_{os}k}{2} & 0 & -i(\omega-\omega_0) \end{pmatrix} \begin{pmatrix} n_{e1}(\omega) \\ n_{e1}(\omega+\omega_0) \\ n_{e1}(\omega-\omega_0) \\ P_{e1}(\omega) \\ P_{e1}(\omega+\omega_0) \\ P_{e1}(\omega-\omega_0) \end{pmatrix} = \vec{0}. \quad (7)$$

By taking the determinant of the matrix equal to zero, we can get the dispersion relation between ω and k. The wave number of the instability k_m corresponds to the value at which the imaginary part of ω [Im(ω)] is maximal and can be calculated numerically through this dispersion equation. In the following, for simplicity, the moving high-density layer is treated nonrelativistic, and thus the obtained k_m mode and growth rate from the matrix can both be directly used in the laboratory frame.

Figure 2 shows a numerical example. We take $\gamma_0 = 1.06$, $\omega_{pe} = 6.32\omega_0$, $\omega_{pi} = 0.147\omega_0$, and $T_e = 0.005 m_e c^2$. The relation between k and Im(ω) from Eq. (7) is plotted in Fig. 2. One can easily get the most unstable mode of k_m as 27.5 ω_0/c. Besides, there is another peak ($k = 30\omega_0/c$) existing in this mode spectrum. However, the real part of ω [Re(ω)] corresponding to this peak is nonzero and not consistent with the purely growing fluctuations observed in simulations. In the following, we consider only the most unstable k_m with zero frequency [i.e., Re(ω)=0].

It is noted that the electron temperature here is set not very high (i.e., 2.5 keV), as electron heating is quite limited for a nonoscillating ponderomotive force from the CP laser pulse.

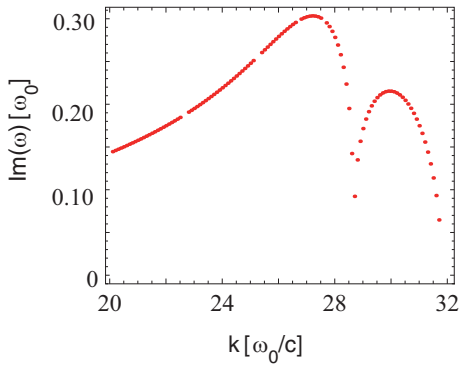

FIG. 2. The relationship between k and Im(ω) obtained from Eq. (7) in the case of $\gamma_0 = 1.06$, $\omega_{pe} = 6.32\omega_0$, $\omega_{pi} = 0.147\omega_0$, and $T_e = 0.005 m_e c^2$.

Besides the ES mode, in the following, we take only the EM mode into consideration. Since the EM mode is actually stimulated by the S-polarization part of the CP laser through the $v \times B$ effect, here for simplicity, $A_{x0} = A_0 \cos(\omega_0 t + \phi)$ (S-polarization part) is adopted as the initial laser vector potential. Then, similarly, all the quantities can be divided into a zero-order part plus a first-order quantity. From the Coulomb gauge, one can get $A_{y1} = 0$. Thus all the first-order equations can be written as

$$\frac{\partial n_{e1}}{\partial t} + n_{e0}\frac{\partial v_{ey1}}{\partial y} = 0, \quad (8a)$$

$$\frac{\partial P_{ey1}}{\partial t} = e\frac{\partial \Phi_1}{\partial y} - ev_{ex0}\frac{\partial A_{x1}}{\partial y} - \frac{1}{n_{e0}}\frac{\partial (n_{e1}T_e)}{\partial y}, \quad (8b)$$

$$\frac{\partial n_{i1}}{\partial t} + n_{i0}\frac{\partial v_{iy1}}{\partial y} = 0, \quad (8c)$$

$$\frac{\partial v_{iy1}}{\partial t} = -\frac{q_i}{m_i}\frac{\partial \Phi_1}{\partial y}, \quad (8d)$$

$$\frac{\partial^2 \Phi_1}{\partial y^2} = -4\pi(q_i n_{i1} - e n_{e1}), \quad (8e)$$

$$\left(\frac{1}{c^2}\frac{\partial^2}{\partial t^2} - \frac{\partial^2}{\partial y^2} + \frac{\omega_{pe}^2}{c^2}\kappa\right)A_{x1} = -\frac{4\pi}{c}e n_{e1} v_{ex0}. \quad (8f)$$

From Eqs. (8), $v_{ex0}\frac{\partial A_{x1}}{\partial y}$, corresponding to $v_{ex0}B_{z1}$, is the first order of ponderomotive force that leads to the instability. Therefore, the S-polarization part of a CP laser stimulates only the EM mode. By using the standard Fourier analysis as mentioned above, we can finally obtain the relation between n_{e1} and A_{x1}:

$$\left(\frac{T_e}{n_{e0}}k - \frac{\omega^2}{kn_{e0}\kappa} - \frac{4\pi}{k}\frac{\omega^2}{\omega_{pi}^2 - \omega^2}\right)n_{e1}(\omega) + \frac{kv_{os}}{2}[A_{x1}(\omega+\omega_0) + A_{x1}(\omega-\omega_0)] = 0, \quad (9a)$$

$$\zeta(\omega)A_{x1}(\omega) - 2\pi v_{os}[n_{e1}(\omega+\omega_0) + n_{e1}(\omega-\omega_0)] = 0, \quad (9b)$$

where $\zeta(\omega) = \omega^2 - k^2 - \omega_{pe}^2\kappa$. Similarly, by replacing ω with $\omega \pm \omega_0$ and ignoring the components at $2\omega_0$, one can get another four equations:

$$\left[\frac{T_e}{n_{e0}}k - \frac{(\omega+\omega_0)^2}{kn_{e0}\kappa} + \frac{4\pi}{k}\right]n_{e1}(\omega+\omega_0) + \frac{kv_{os}}{2}[A_{x1}(\omega)] = 0, \tag{10a}$$

$$\left[\frac{T_e}{n_{e0}}k - \frac{(\omega-\omega_0)^2}{kn_{e0}\kappa} + \frac{4\pi}{k}\right]n_{e1}(\omega-\omega_0) + \frac{kv_{os}}{2}[A_{x1}(\omega)] = 0, \tag{10b}$$

$$\zeta(\omega+\omega_0)A_{x1}(\omega+\omega_0) - 2\pi v_{os}[n_{e1}(\omega)] = 0, \tag{10c}$$

$$\zeta(\omega-\omega_0)A_{x1}(\omega-\omega_0) - 2\pi v_{os}[n_{e1}(\omega)] = 0. \tag{10d}$$

These six closed equations show the relationship between n_{e1} and A_{x1} at three frequencies $(\omega, \omega \pm \omega_0)$, and the corresponding coefficient matrix is

$$\begin{pmatrix}
\frac{T_e}{n_{e0}}k - \frac{\omega^2}{kn_{e0}\kappa} - \frac{4\pi}{k}\frac{\omega^2}{\omega_{pi}^2-\omega^2} & 0 & 0 & 0 & \frac{kv_{os}}{2} & \frac{kv_{os}}{2} \\
0 & \frac{T_e}{n_{e0}}k - \frac{(\omega+\omega_0)^2}{kn_{e0}\kappa} + \frac{4\pi}{k} & 0 & \frac{kv_{os}}{2} & 0 & 0 \\
0 & 0 & \frac{T_e}{n_{e0}}k - \frac{(\omega-\omega_0)^2}{kn_{e0}\kappa} + \frac{4\pi}{k} & \frac{kv_{os}}{2} & 0 & 0 \\
0 & -2\pi v_{os} & -2\pi v_{os} & \zeta(\omega) & 0 & 0 \\
-2\pi v_{os} & 0 & 0 & 0 & \zeta(\omega+\omega_0) & 0 \\
-2\pi v_{os} & 0 & 0 & 0 & 0 & \zeta(\omega-\omega_0)
\end{pmatrix}. \tag{11}$$

After further derivation, it is equivalent to solve the determinate of a matrix as

$$\begin{pmatrix}
\frac{T_e}{n_{e0}}k - \frac{\omega^2}{kn_{e0}\kappa} - \frac{4\pi}{k}\frac{\omega^2}{\omega_{pi}^2-\omega^2} & \frac{kv_{os}}{2} & \frac{kv_{os}}{2} \\
-2\pi v_{os} & \zeta(\omega+\omega_0) & 0 \\
-2\pi v_{os} & 0 & \zeta(\omega-\omega_0)
\end{pmatrix}. \tag{12}$$

Taking its determinant equal to zero, we can get the dispersion relation. Figure 3 shows a numerical example. We take $\gamma_0 = 1.06$, $\omega_{pe} = 6.32\omega_0$, $\omega_{pi} = 0.147\omega_0$, and $T_e = 0.005m_ec^2$, the same as Fig. 2. The relation between k and (Imω) from Eq. (12) is plotted in Fig. 3. One can easily get the value of k_m as 1.4 ω_0/c. The maximal Im(ω) of EM mode is about 0.0334 ω_0, much smaller than that of ES mode (0.3 ω_0) for the same laser plasma paramters, which indicates that the ES mode dominates the whole development of the transverse instability.

For accurate descriptions, one needs to take all these modes into account. Based on the full set equations [Eqs. (1)] and initial conditions of $A_{x0} = A_0\sin(\omega_0 t + \phi)$, $A_{y0} = A_0\cos(\omega_0 t + \phi)$ for a CP laser. After similar processing as mentioned above (linearization and spatio-temporal Fourier transformation), we can finally get nine closed equations for nine quantities (n_{e1}, P_{ey1}, and A_{x1} at ω and $\omega \pm \omega_0$), and the coefficient matrix is written as

$$\begin{pmatrix}
-\omega & kv_{os}/2 & kv_{os}/2 & kn_{e0}\kappa & 0 & 0 & 0 & 0 & 0 \\
kv_{os}/2 & -\omega-\omega_0 & 0 & 0 & kn_{e0}\kappa & 0 & 0 & 0 & 0 \\
kv_{os}/2 & 0 & -\omega+\omega_0 & 0 & 0 & kn_{e0}\kappa & 0 & 0 & 0 \\
-i\epsilon(\omega) & 0 & 0 & -\omega & kv_{os}/2 & kv_{os}/2 & 0 & -ikv_{os}/2 & ikv_{os}/2 \\
0 & 4\pi/k + kT_e/n_{e0} & 0 & kv_{os}/2 & -\omega-\omega_0 & 0 & ikv_{os}/2 & 0 & 0 \\
0 & 0 & 4\pi/k + kT_e/n_{e0} & kv_{os}/2 & 0 & -\omega+\omega_0 & -ikv_{os}/2 & 0 & 0 \\
0 & 2i\pi v_{os} & -2i\pi v_{os} & 0 & 0 & 0 & \zeta(\omega) & 0 & 0 \\
-2i\pi v_{os} & 0 & 0 & 0 & 0 & 0 & 0 & \zeta(\omega+\omega_0) & 0 \\
2i\pi v_{os} & 0 & 0 & 0 & 0 & 0 & 0 & 0 & \zeta(\omega-\omega_0)
\end{pmatrix}. \tag{13}$$

The dispersion relation can be obtained by taking the determinant of Eq. (13) equal to zero. Figure 4 shows a typical example of this case. The initial parameters are set as $\gamma_0 = 1.5$, $\omega_{pe} = 6\omega_0$, $\omega_{pi} = 0.13\omega_0$, and $T_e = 0.005m_ec^2$. The relation between k and Im(ω) is presented in Fig. 4. One can see the curves from Eq. (7) (solid blue) and Eq. (13) (dashed red) have very similar trends, and the obtained k_m are both close to $7.2\omega_0/c$, which indicates that the ES mode is more effective than the EM mode. Besides this example, we also have scanned in a wide range of parameters and found that the ES mode still dominates in all cases. In the following, for simplicity, only the electrostatic effect is considered and the electron temperature is ignored.

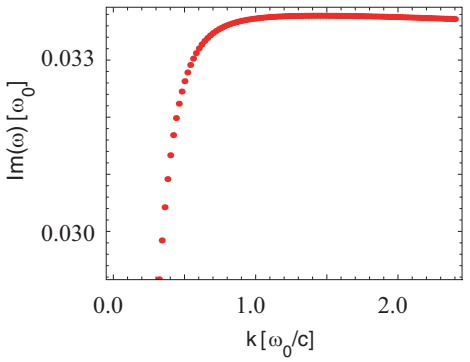

FIG. 3. The relationship between k and Im(ω) obtained from Eq. (12) in the case of $\gamma_0 = 1.06$, $\omega_{pe} = 6.32\omega_0$, $\omega_{pi} = 0.147\omega_0$, and $T_e = 0.005 m_e c^2$.

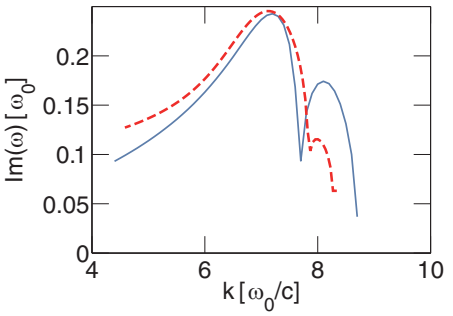

FIG. 4. The relationship between k and Im(ω) obtained from Eq. (7) (solid blue) and Eq. (13) (dashed red) in the case of $\gamma_0 = 1.5$, $\omega_{pe} = 6\omega_0$, $\omega_{pi} = 0.13\omega_0$, and $T_e = 0.005 m_e c^2$.

III. TRANSVERSE INSTABILITY FOR $a_0 < 1$

For $a_0 < 1$ taking $\kappa \approx 1$ for nonrelativistic electrons, the dispersion relation can be calculated as

$$\begin{aligned} &-4\omega^8 + 4\omega^6\left(\xi^2 + 2\omega_0^2 + 3\omega_{pe}^2 + \omega_{pi}^2\right) + \omega^4\left[-\xi^4 - 4\xi^2\left(\omega_0^2 - \omega_{pe}^2\right)^2 - 4\left(\omega_0^4 + 3\omega_{pe}^4 + 2\omega_0^2\omega_{pi}^2 + 2\omega_{pe}^2 + \omega_{pi}^2\right)\right] \\ &+\omega^2\left\{\xi^2\left(\omega_{pe}^2 + \omega_{pi}^2\right) + 4\left(\omega_0^2 - \omega_{pe}^2\right)^2\left(\omega_{pe}^2 + \omega_{pi}^2\right) + 2\xi^2\left[-2\omega_{pe}^4 + \omega_{pe}^2\omega_{pi}^2 + 2\omega_0^2\left(\omega_{pe}^2 + \omega_{pi}^2\right)\right]\right\} \\ &-\xi^2\omega_{pe}^2\omega_{pi}^2\left(\xi^2 + 2\omega_0^2 - 2\omega_{pe}^2\right) = 0. \end{aligned} \tag{14}$$

where $\xi = k v_{os}$. To simplify Eq. (14), several assumptions based on numerical simulations are given as follows:

1. The maximal Im(ω) corresponds to the case where Re(ω) = 0.

2. The maximal growth rate $\gamma_m = \mathrm{Im}(\omega)$ is on the same order of ω_{pi}

3. $\xi = k v_{os}$ for maximum growth rate is on the same order of ω_{pe}.

Therefore, we may drop all the components including ω^8 and ω^6 and keep only dominant coefficients of ω^4, ω^2 and constant terms. Equation (14) can then be simplified significantly as

$$\begin{aligned} &\omega^4\left(\xi^4 + 12\omega_{pe}^4\right) - \omega^2\omega_{pe}^2\left(\xi^2 - 2\omega_{pe}^2\right)^2 \\ &+\xi^2\omega_{pe}^2\omega_{pi}^2\left(\xi^2 - 2\omega_{pe}^2 + 2\omega_0^2\right) = 0. \end{aligned} \tag{15}$$

In order to show the similarity of Eqs. (15) and (14), a series of numerical simulations were carried out. Figure 5 gives an example. We take $\gamma_0 = 1.5$, $\omega_{pe} = 6.32\omega_0$, and $\omega_{pi} = 0.147\omega_0$. The relations between ξ and ω from Eq. (14) (solid blue) and Eq. (15) (dashed yellow) are plotted in Figs. 5(a) and 5(b). One can find the two curves have good agreement with each other.

In most cases, $\omega_{pe} \gg \omega_0 > \omega_{pi}$. ξ for the maximum |Im(ω)| can be directly solved from Eq. (15) as $\xi_{\max} \approx \sqrt{2}\omega_{pe}$, and the instability mode wave number k_m is

$$k_m = \frac{\xi_{\max}}{v_{os}} \approx \frac{\sqrt{2}\omega_{pe}}{v_{os}}. \tag{16}$$

In previous studies, self-consistent analytical models have been developed to describe nonlinear effects such as density compression and induced transparency in the case of a high-intensity laser interaction with overdense plasma [43]. Besides the relatively complicated analysis, the expression of ω_{pe} can be easily obtained by using the following kinetic model, and assuming an uniform density profile and charge neutrality (i.e., $n_e \approx n_i$) within the high-density layer. The basic physical picture of the hole boring process for $a_0 < 1$ in the longitudinal direction is shown in Fig. 6, as mentioned in a number of papers [13,18].

Based on the assumptions, the electrostatic field E_s can be expressed as $E_s = E_{s0}(l_s - z)$, $(0 < z < l_s)$, where E_{s0} is the maximum longitudinal electrostatic field and l_s is the thickness of this layer. After balance is built, the equilibrium between the laser pressure and the electrostatic force within the layer can be written as $\frac{1}{2}E_{s0}e\bar{n}_e l_s = 2I/c$, where I is the laser intensity and $\bar{n}_e$ is the averaged electron density of the high-density layer. Meanwhile, in the comoving frame, ions ($Z = 1$) are moving into this region with a velocity of $v = -v_b$ and then be decelerated to $v = 0$ at the boundary (the O point). So we

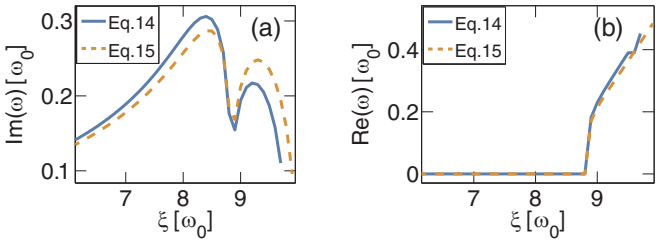

FIG. 5. The relations between ξ and ω from Eq. (14) (solid blue) and Eq. (15) (dashed yellow) in the case of $\gamma_0 = 1.5$, $\omega_{pe} = 6.32\ \omega_0$, and $\omega_{pi} = 0.147\ \omega_0$.

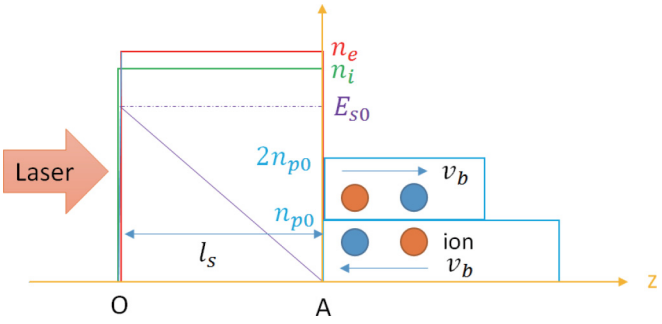

FIG. 6. Schematic drawing of the hole boring process for $a_0 < 1$. Here n_{p0} is the initial plasma density.

can get $\frac{1}{2}E_{s0}el_s = \frac{1}{2}m_i v_b^2$. Combing these two equations, the first relation between ions and laser pressure is

$$\frac{1}{2}\bar{n}_e m_i v_b^2 = \frac{2I}{c}. \tag{17}$$

As the balance is dynamic, ions are moving into the high-density layer with $n = n_{p0}$ and $v = -v_b$ and also out with $n = n_{p0}$ and $v = v_b$ consecutively. During δt, the ion momentum conversation leads to $(2I/c)\delta t = n_{p0}v_b\delta t(v_b + v_b)$, which is

$$2n_{p0}m_i v_b^2 = \frac{2I}{c}. \tag{18}$$

Combing Eqs. (17) and (18), one can get

$$\bar{n}_e = \bar{n}_i = 4n_{p0}. \tag{19}$$

This simple relation can be readily verified by PIC simulations.

On the other hand, by applying the Fresnel-like boundary condition and neglecting the $v_b \times B$ effect in the y direction ($v_b \ll c$), we can get

$$v_{os}/c \approx 2a_0\frac{\omega_0}{\omega_{pe}}. \tag{20}$$

With the new form of v_{os} [Eq. (20)] and ω_{pe} [Eq. (19)], Eq. (16) can be written in a form easier for direct comparison with PIC simulations:

$$k_m \approx 2\sqrt{2}\frac{n_{p0}}{a_0 n_c}[\omega_0/c]. \tag{21}$$

To verify the above theory, we performed a series of 2D PIC simulations using the code OSIRIS [44]. In these simulations, a CP laser driver with a transverse uniform profile is used. The laser has a flattop temporal profile and propagates in the z direction. High resolutions are used in both directions ($\Delta y = \Delta z = 0.002\ c\omega_0^{-1}$), with 16 particles per species in each cell. The foil is a pure hydrogen plasma with a step density profile.

Figure 7 shows an example. We take $a_0 = 0.2$ and $n_{p0} = 10n_c$. In Fig. 7(a), one can see ion density ripples are induced in the high-density layer at the time of $t = 180\omega_0^{-1}$ after the laser impinges on the target. A line out corresponding with the red dot line of Fig. 7(a) is presented, showing the periodic density structures appearing during the interaction process. Figure 7(b) is the 2D Fourier transformation of Fig. 7(a), and a line out showing the distribution of k_y at $k_z = 0$ corresponding with the green dot line is also presented. The obtained instability mode number k_m is about 125 ω_0/c, in good agreement with

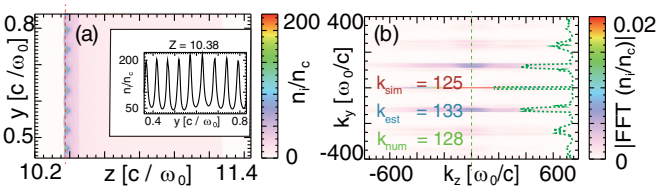

FIG. 7. The ion density fluctuations at $t = 180\omega_0^{-1}$ after laser impinges on the target in the case of $a_0 = 0.2$, $n_{p0} = 10n_c$. (a) The ion density with transverse ripples within the front high-density layer and its line-out distribution at $z = 10.38\ c/\omega_0$ (the red dot line). (b) The FFT of the proton density and its line-out distribution at $k_z = 0$ (the green dot line). $k_{\rm sim}$, $k_{\rm num}$, and $k_{\rm est}$ are obtained from PIC simulations, from direct numerical solutions of Eq. (7), and from Eq. (21), respectively.

the estimated value $k_{\rm est}$ (133 ω_0/c) from Eq. (21) and numerical value $k_{\rm num}$ (128 ω_0/c) from Eq. (7).

Besides this typical example, we also scanned in a wide range of parameters to show the validity of this theory. Figure 8(a) plots the relation between k_m and a_0 by fixing the initial plasma density ($n_{p0} = 10n_c$). Three values of k_m [k_m obtained from PIC simulation, from direct numerical solution of Eq. (7), and from Eq. (21)] are used for comparison. One can see very good agreements are obtained. In Fig. 8(b) we also plot the relation between k_m and n_{p0} by fixing $a_0 = 0.2$. One can see equally good agreements between the three values of k_m.

The growth rate γ_{m0} at k_m can also be obtained from Eq. (15) directly:

$$\gamma_{m0} \approx 2\ \omega_{pi}. \tag{22}$$

We performed a series of 2D simulations with a large range of plasma parameters similar to Fig. 8 to confirm our analysis. Figure 9(a) gives the relation between γ_m and a_0 at $n_{p0} = 10n_c$. It is found that though γ_m is varying with a_0, it is still on the same order of ω_{pi} (in the range of $\omega_{pi} \sim 2\omega_{pi}$), which has some agreements with Eq. (22).

The weak relation between γ_m and a_0 mainly comes from the fact that in the comoving frame, ions are moving in and out of the high-density layer consecutively, and this area is not stationary. If the longitudinal flow is quite slow, the expression of growth rate γ_m can also be evaluated. We assume that at $t = t_0$, the ion density fluctuation is $f(t_0) = \delta n_0 l_s$,

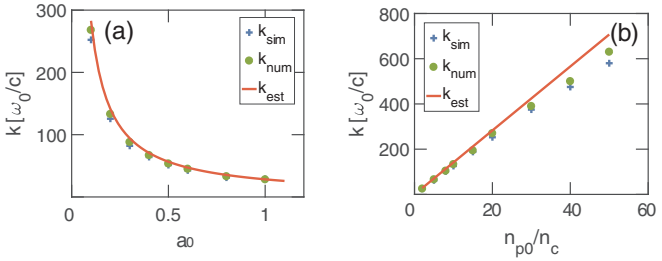

FIG. 8. (a) The relationship between k_m and a_0 for $n_{p0} = 10n_c$. (b) The relationship between k_m and n_{p0} for $a_0 = 0.2$. $k_{\rm sim}$, $k_{\rm num}$, and $k_{\rm est}$ are obtained from PIC simulations, from direct numerical solutions of Eq. (7), and from Eq. (21), respectively.

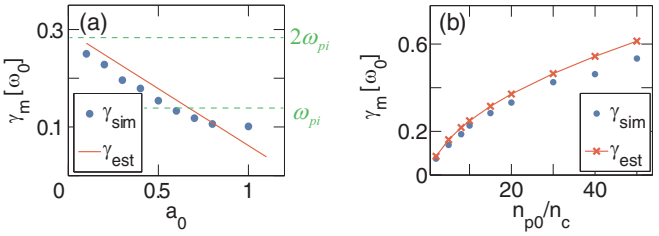

FIG. 9. (a) The relationship between γ_m and a_0 at $n_{p0} = 10n_c$. (b) The relationship between γ_m and n_{p0} at $a_0 = 0.2$. $\gamma_{\rm est}$ and $\gamma_{\rm sim}$ are the estimated and simulation growth rates of ion density ripples, respectively.

where l_s is the length of the high-density layer, and δn_0 is the ion density fluctuation at $t = t_0$. Then at $t = t_0 + \delta t$, the fluctuation becomes as $f(t_0 + \delta t) = \delta n_0 e^{\gamma_{m0}\delta t}(l_s - v_b\delta t)$. The growth rate can be calculated as $e^{\gamma_m \delta t} = f(t_0 + \delta t)/f(t_0)$, where $v_b = a_0 c\sqrt{m_e n_c/m_i n_{p0}}$ is the hole boring velocity of ions in nonrelativistic regime. Based on the analysis above, it is straightforward to obtain

$$\gamma_m \approx 2\omega_{pi} - 2\omega_{0i}\eta a_0, \tag{23}$$

where $\omega_{0i} = \sqrt{m_e/m_i}\omega_0$ is the critical ion plasma frequency, and η is a coefficient. Equation (23) shows γ_m has a weakly linear dependence on a_0, which is in quite good agreement with Fig. 9(a) for $a_0 < 0.7$. And $\eta \approx 4.8$ can be evaluated from simulations. It is noted that Eq. (23) is valid for the initial several $1/\omega_{pi}$, since as the instability grows, more other effects like electron heating and radiation pressure transverse nonuniformity will get involved. To guarantee that the ion flow is slow enough, a_0 also should be quite small.

As Fig. 9(b) shows, if we fix $a_0 = 0.2$, the values of growth rates from simulations also have great agreement with that from Eq. (23).

IV. TRANSVERSE INSTABILITY FOR $a_0 > 1$

For $a_0 > 1$, the Lorenz factor of electrons needs to be considered. In this case, if $\sqrt{\kappa}\omega_{pe} \gg \omega_0$, Eq. (7) can also be simplified into a similar type as Eq. (15):

$$\omega^4\left(\xi^4 + 12\kappa^2\omega_{pe}^4\right) - \kappa\omega^2\omega_{pe}^2\left(\xi^2 - 2\kappa\omega_{pe}^2\right)^2 + \xi^2\kappa\omega_{pe}^2\omega_{pi}^2\left(\xi^2 - 2\kappa\omega_{pe}^2 + 2\omega_0^2\right) = 0. \tag{24}$$

And one can obtain k_m:

$$k_m \approx \sqrt{2}\frac{\omega_{pe}}{v_{os}}\sqrt{\kappa} = \frac{\omega_{pe}}{\sqrt{\gamma_0}}\sqrt{\frac{\gamma_0^2+1}{\gamma_0^2-1}}. \tag{25}$$

Equation (25) is valid both for thick foil cases (hole boring) and thin foils cases (light sail). In the following, we present detailed theoretical analysis [based on Eq. (25)] of the transverse instabilities happening in these two regimes, and 2D PIC simulations are systematically performed to verify the obtained formulas.

A. Hole boring regime

In this case, if the laser is not very intense (i.e., the ion depletion layer is much shorter than the compressed layer composed of ions and electrons), we can still take the entire ion high-density layer as a whole and assume a uniform density profile (here $n_e \neq n_i$). In order to obtain the estimation of ω_{pe} and γ_0, several relations needs to be derived. First, according to a Fresnel-like boundary condition similar to Eq. (20), one can get

$$\sqrt{\gamma_0^2 - 1} = 2a_0\frac{\omega_0}{\omega_{pe}}\sqrt{\gamma_0}. \tag{26}$$

Then, by using the same model as Eqs. (17)–(19), one can get the formulas of $\bar{n}_e$ and $\bar{n}_i$ within the high-density layer as $\bar{n}_e = 4n_{p0}(l_s + l_d)/l_s$ and $\bar{n}_i = 4n_{p0}$, where l_s, l_d are the lengths of compressed and depletion layers, respectively.

Finally, combining the above three equations with the Poisson equation, one can get two simple expressions of the relations between γ_0 and n_e as

$$\gamma_0 - \frac{1}{\gamma_0} = 4a_0^2\frac{n_c}{n_e}, \tag{27a}$$

$$\frac{n_e - 4n_{p0}}{n_c} = \frac{a_0^2}{\gamma_0}. \tag{27b}$$

From Eqs. (27), $\omega_{pe} = \omega_0\sqrt{n_e/n_c}$ and γ_0 can be directly calculated, and thus k_m can also be estimated.

In order to verify the above analysis, we performed a series of 2D PIC simulations. Figure 10 gives a typical example. In this simulation, a CP laser with $a_0 = 5$ is used to interact with a thick target with initial plasma density of $n_{p0} = 10\ n_c$ and a thickness of $d = 5\ c/\omega_0$. In Fig. 10(a) one can see the ion density ripples are formed in the high-density layer at the ront surface during the RPA process. After 2D FFT processing, as shown in Fig. 10(b), a specific k_y mode grows the fastest with the value of 4.34 ω_0/c, which has good agreement with the estimated value 5.46 ω_0/c from Eqs. (27) and Eq. (25), and the numerical value 4.84 ω_0/c from Eq. (7).

In Fig. 11(a) we plot the relation between k_m and a_0 by fixing the plasma density ($n_{p0} = 20\ n_c$). One can see the three values of k_m [k_m obtained from PIC simulation, from direct numerical solution of Eq. (7), and from Eqs. (27) and Eq. (25)] have very good agreement. In Fig. 11(b) we also plot the relation between k_m and n_{p0} by fixing $a_0 = 5$. One can see the three values of k_m are still very close to each other in a wide range of plasma densities, and the ratio between $k_{\rm sim}$ and $k_{\rm est}$ is about 70%–80%.

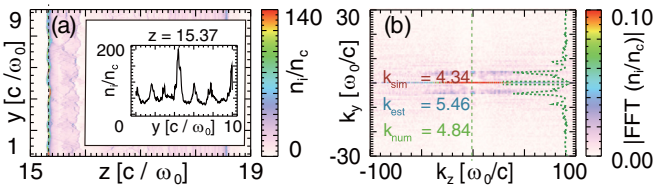

FIG. 10. The ion density fluctuations at $t = 120\omega_0^{-1}$ after the laser impinges on the target in the case of $a_0 = 5, n_{p0} = 10\ n_c$. (a) The ion density transverse ripples within the high-density layer and its line-out distribution at $z = 15.37\ c/\omega_0$ (the black dot line). (b) The FFT of the ion density and its line-out distribution at $k_z = 0$ (the green dot line). $k_{\rm sim}$, $k_{\rm num}$, and $k_{\rm est}$ are obtained from PIC simulations, from direct numerical solutions of Eq. (7), and from Eq. (25), respectively.

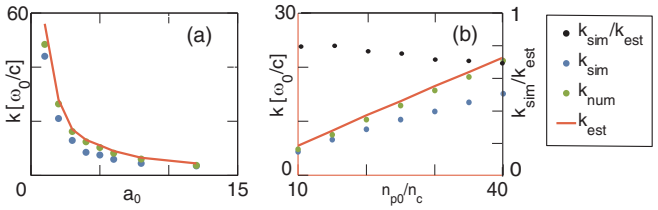

FIG. 11. (a) The relationship between k_m and a_0 when $n_{p0} = 20\ n_c$. (b) The relationship between k_m and n_{p0} when $a_0 = 5$. $k_{\rm sim}$, $k_{\rm num}$, and $k_{\rm est}$ are obtained from PIC simulations, from direct numerical solutions of Eq. (7), and from Eq. (25), respectively.

The small differences mainly come from the fact that n_i is not exactly $4n_{p0}$ ($n_i < 4n_{p0}$).

It is noted that Eqs. (27) are most reasonable in the case of $l_d \ll l_s$ that ions (electrons) can still be treated as a single layer. From performed simulations, it is found that the condition needs to roughly satisfy $l_d \leqslant 1/4\ l_s$, which can also be approximately written as $a_0^2 \leqslant (n_{p0}/n_c)\gamma_0$. If the laser intensity is very high such that the electrons are pushed forward fiercely, leaving behind majority ions, Eqs. (27) are not valid any more. In this case, we may evaluate ω_{pe} only from simulations and then calculate γ_0 from Eq. (26).

Figure 12 shows an example of this case. We begin with $a_0 = 5$, $n_{p0} = 3\ n_c$, and $d = 20\ c/\omega_0$. In this simulation, the laser pressure is so strong that ($l_d \leqslant 1/4\ l_s$) is not satisfied. Thus we can estimate $n_e \approx 20\ n_c$ only from simulations. Then the obtained mode number $k_{\rm num} = 1.7\ \omega_0/c$ from numerical solutions of Eq. (7) and $k_{\rm est} = 2.1\ \omega_0/c$ from estimations of Eq. (25) have good agreements with the simulation result of $2.0\ \omega_0/c$. If applying Eqs. (27), we get $k_{\rm num} = 0.8\ \omega_0/c$ and $k_{\rm est} = 1.4\ \omega_0/c$, which seems quite distinctive from the simulation results.

The extremity of k_m can also be approximately estimated if we combine Eqs. (26) and (25) into a new form:

$$k_m = \frac{2a_0}{\sqrt{\gamma_0^2 - 1}}\sqrt{\frac{\gamma_0^2 + 1}{\gamma_0^2 - 1}}. \tag{28}$$

Since $|\gamma_0|_{\rm max}$ approximately equals a_0 in most simulations for high-laser intensity in the HB regime, from Eq. (28) one gets $|k_m|_{\rm min} \sim 2$. Several 2D PIC simulations have been performed to verify this interesting trend. The results are shown in Table I.

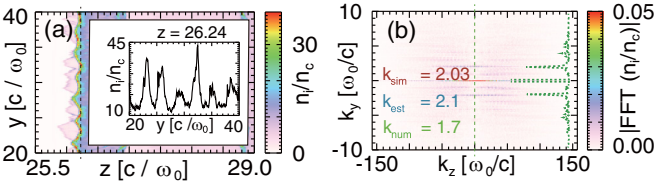

FIG. 12. The ion density fluctuations at $t = 200\omega_0^{-1}$ after laser impinges on the target in the case of $a_0 = 5$ and $n_{p0} = 3\ n_c$. (a) The ion density transverse ripples within the front high-density layer and its line-out distribution at 26.24 c/ω_0. (b) The FFT of the ion density and its line-out distribution at $k_z = 0$ (the green dot line). $k_{\rm sim}$, $k_{\rm num}$, and $k_{\rm est}$ are obtained from PIC simulations, from direct numerical solutions of Eq. (7), and from Eq. (25), respectively.

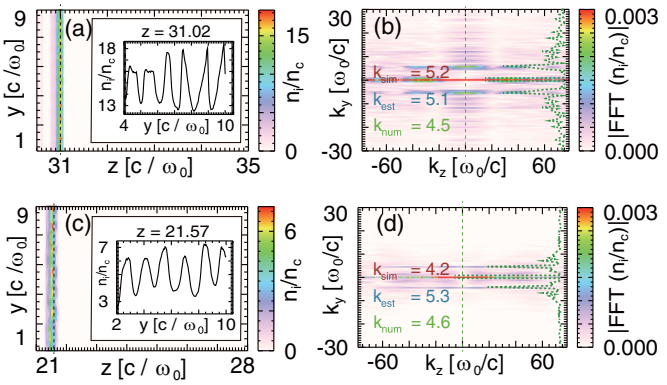

FIG. 13. The ion density evolution in the case of $a_0 = 2.5$, $n_{p0} = 10\ n_c$, $d = 0.4\ c/\omega_0$ at $t = 100\omega_0^{-1}$ after the laser impinges on the target (a, b) and in the case of $a_0 = 1$, $n_{p0} = 4\ n_c$, $d = 0.4\ c/\omega_0$ at $t = 150\omega_0^{-1}$ after the laser impinges on the target (c, d). (a, c) The ion density distributions and their line-out distribution at $z = 31.02\ c/\omega_0$ for (a) and $21.57\ c/\omega_0$ for (c) (the black dot line). (b, d) The FFT of the ion density and its line-out distribution at $k_z = 0$ (the green dot line). $k_{\rm sim}$, $k_{\rm num}$, and $k_{\rm est}$ are obtained from PIC simulations, from direct numerical solutions of Eq. (7), and from Eq. (25), respectively.

B. Light sail regime

In the light sail process, a ultrathin foil is pushed and accelerated by the laser pressure as a whole, and at the same time the laser can partially propagate through it. Equation (25) can still be valid in this case. However, ω_{pe} and γ_0 need to be evaluated from simulations. To show the developments of transverse instabilities and the related mode structures during the LS regime, two 2D PIC simulations are presented in Fig. 13.

In Figs. 13(a) and 13(b), we set the input parameters as $a_0 = 2.5$, $n_{p0} = 10\ n_c$, and $d = 0.4\ c/\omega_0$. At the time of $t = 100\omega_0^{-1}$ after laser impinges on the target, one can see density ripples are induced in the whole target [Fig. 13(a)], and the mode wave number in this simulation is $5.2\ \omega_0/c$, which is quite similar to the estimated value $5.1\ \omega_0/c$ from Eq. (25) and numerical value 4.5 from Eq. (7) [Fig. 13(b)]. In Figs. 13(c) and 13(d), we set the input parameters as $a_0 = 1$, $n_{p0} = 4\ n_c$, and $d = 0.4\ c/\omega_0$. The mode wave number in this simulation is $4.2\ \omega_0/c$, which is quite close to the estimated value $5.3\ \omega_0/c$ from Eq. (25) and numerical value 4.6 from Eq. (7) [Fig. 13(d)].

It is noted that for a very intense laser ($a_0 \gg 1$), the expression of the k_m mode will be simplified as $k_m \approx \omega_{pe}/\sqrt{\gamma_0}$ and approaching to 1 (i.e., $|k_m|_{\rm min} \approx 1$) due to the relation $\omega_{pe} \geqslant \sqrt{\gamma_0}$.

TABLE I. 2D PIC simulation results in cases of $a_0/n_{p0} \geqslant 1$.

Simulation parameters	$k_{\rm sim}[\omega_0/c]$
$a_0 = 10$, $n_{p0} = 10n_c$, $d = 20\ c/\omega_0$	1.9
$a_0 = 15$, $n_{p0} = 10n_c$, $d = 20\ c/\omega_0$	1.78
$a_0 = 20$, $n_{p0} = 20n_c$, $d = 20\ c/\omega_0$	1.88
$a_0 = 30$, $n_{p0} = 20n_c$, $d = 30\ c/\omega_0$	1.74

V. CONCLUSIONS

In summary, transverse stability plays a crucial role for obtaining high-quality ion beams using the RPA scheme. In this paper we present a one-dimensional theoretical model to explain the intrinsic physical mechanism of the transverse density ripples induced in the RPA process. It turns out that the instability mainly originates from the strong coupling between transverse oscillating electrons and quasistatic ions via the ponderomotive force with spatial variations. The theory contains a fully treatment of both electrostatic (ES) and electromagnetic (EM) modes and confirms that the ES mode actually dominates the whole RPA process at the early linear stage.

The predictions of the mode structure and growth rate have good agreement with 2D PIC simulations for a wide range of laser powers (laser a_0 from 0.1 to 30, corresponding to currently available TW to PW lasers). The discussed target densities in the paper (from $4n_c$ to $50n_c$) are chosen for the consideration of limited computational amounts and relatively lower than real solid targets. However, the basic physical mechanism should be the same even for densities up to 100–1000n_c, and simulations show that in the case, similar mode structures can still be observed and are well consistent with our estimations. Besides, in all the simulations mentioned above, we adopt uniform laser intensity profiles for the exact comparison with the theoretical model. For realistic cases of laser pulses with nonuniform transverse profiles like Gaussian [e.g., $\exp(-r^2/w_0^2)$], density ripples with predicted mode structures can still appear and grow in the central region of the high-density layer as shown in the simulations of Ref. [40].

This theory is based on a dispersion relation analysis and mainly suitable to describe the origin of transverse instability at the early linear stage of several $1/\omega_{pi}$. Once coming into the nonlinear stage, significant distortion of the target and electron heating effect can become crucial, leading to several other kinds of instabilities involved in the latter process.

ACKNOWLEDGMENTS

This work was supported by NSFC Grants No. 11425521, No. 11535006, No. 11475101 and No. 11775125, the Thousand Young Talents Program. Simulations were performed on the Sunway TaihuLight cluster at National Supercomputing Center and Edison cluster at NERSC.

[1] R. A. Snavely, M. H. Key, S. P. Hatchett, T. E. Cowan, M. Roth, T. W. Phillips, M. A. Stoyer, E. A. Henry, T. C. Sangster, M. S. Singh, S. C. Wilks, A. MacKinnon, A. Offenberger, D. M. Pennington, K. Yasuike, A. B. Langdon, B. F. Lasinski, J. Johnson, M. D. Perry, and E. M. Campbell, Phys. Rev. Lett. **85**, 2945 (2000).

[2] H. Daido, M. Nishiuchi, and A. S. Pirozhkov, Rep. Prog. Phys. **75**, 056401 (2012).

[3] A. Macchi, M. Borghesi, and M. Passoni, Rev. Mod. Phys. **85**, 751 (2013).

[4] M. Borghesi, S. Bulanov, D. H. Campbell, R. J. Clarke, T. Z. Esirkepov, M. Galimberti, L. A. Gizzi, A. J. MacKinnon, N. M. Naumova, F. Pegoraro, H. Ruhl, A. Schiavi, and O. Willi, Phys. Rev. Lett. **88**, 135002 (2002).

[5] A. J. Mackinnon, P. K. Patel, M. Borghesi, R. C. Clarke, R. R. Freeman, H. Habara, S. P. Hatchett, D. Hey, D. G. Hicks, S. Kar, M. H. Key, J. A. King, K. Lancaster, D. Neely, A. Nikkro, P. A. Norreys, M. M. Notley, T. W. Phillips, L. Romagnani, R. A. Snavely, R. B. Stephens, and R. P. J. Town, Phys. Rev. Lett. **97**, 045001 (2006).

[6] C. K. Li, F. H. Seguin, J. A. Frenje, J. R. Rygg, R. D. Petrasso, R. P. J. Town, P. A. Amendt, S. P. Hatchett, O. L. Landen, A. J. Mackinnon, P. K. Patel, V. A. Smalyuk, T. C. Sangster, and J. P. Knauer, Phys. Rev. Lett. **97**, 135003 (2006).

[7] S. V. Bulanov, T. Z. Esirkepov, V. S. Khoroshkov, A. V. Kunetsov, and F. Pegoraro, Phys. Lett. A **299**, 240 (2002).

[8] V. Malka, S. Fritzler, E. Lefebvre, E. d'Humieres, R. Ferrand, G. Grillon, C. Albaret, S. Meyroneinc, J. P. Chambaret, A. Antonetti, and D. Hulin, Med. Phys. **31**, 1587 (2004).

[9] V. Y. Bychekov, W. Rozmus, A. Maksimchuk, D. Umstadter, and C. E. Capjack, Plasma Phys. Rep. **27**, 1017 (2001).

[10] M. Roth, T. E. Cowan, M. H. Key, S. P. Hatchett, C. Brown, W. Fountain, J. Johnson, D. M. Pennington, R. A. Snavely, S. C. Wilks, K. Yasuike, H. Ruhl, P. Pegoraro, S. V. Bulanov, E. M. Campbell, M. D. Perry, and H. Powell, Phys. Rev. Lett. **86**, 436 (2001).

[11] S. Atzeni, M. Temporal, and J. J. Honrubia, Nucl. Fusion **42**, L1 (2002).

[12] T. Esirkepov, M. Borghesi, S. V. Bulanov, G. Mourou, and T. Tajima, Phys. Rev. Lett. **92**, 175003 (2004).

[13] A. Macchi, F. Cattani, T. V. Liseykina, and F. Cornolti, Phys. Rev. Lett. **94**, 165003 (2005).

[14] X. M. Zhang, B. F. Shen, X. M. Li, Z. Y. Jin, and F. C. Wang, Phys. Plasmas **14**, 073101 (2007).

[15] A. P. L. Robinson, M. Zepf, S. Kar, R. G. Evans, and C. Bellei, New J. Phys. **10**, 013021 (2008).

[16] O. Klimo, J. Psikal, J. Limpouch, and V. T. Tikhonchuk, Phys. Rev. ST Accel. Beams **11**, 031301 (2008).

[17] X. Q. Yan, C. Lin, Z. M. Sheng, Z. Y. Guo, B. C. Liu, Y. R. Lu, J. X. Fang, and J. E. Chen, Phys. Rev. Lett. **100**, 135003 (2008).

[18] A. P. L. Robinson, P. Gibbon, M. Zepf, S. Kar, R. G. Evans, and C. Bellei, Plasma Phys. Control. Fusion **51**, 024004 (2009).

[19] A. Macchi, S. Veghini, and F. Pegoraro, Phys. Rev. Lett. **103**, 085003 (2009).

[20] Y. Wan, J. F. Hua, C. H. Pai, F. Li, Y. P. Wu, W. Lu, C. J. Zhang, X. L. Xu, C. Joshi, and W. B. Mori, Plasma Phys. Control. Fusion **60**, 044016 (2018).

[21] A. Henig, S. Steinke, M. Schnurer, T. Sokollik, R. Horlein, D. Kiefer, D. Jung, J. Schreiber, B. M. Hegelich, X. Q. Yan, J. Meyer-ter-Vehn, T. Tajima, P. V. Nickles, W. Sandner, and D. Habs, Phys. Rev. Lett. **103**, 245003 (2009).

[22] C. A. J. Palmer, N. P. Dover, I. Pogorelsky, M. Babzien, G. I. Dudnikova, M. Ispiriyan, M. N. Polyanskiy, J. Schreiber, P. Shkolnikov, V. Yakimenko, and Z. Najmudin, Phys. Rev. Lett. **106**, 014801 (2011).

[23] S. Kar, K. F. Kakolee, B. Qiao, A. Macchi, M. Cerchez, D. Doria, M. Geissler, P. McKenna, D. Neely, J. Osterholz, R. Prasad, K. Quinn, B. Ramakrishna, G. Sarri, O. Willi, X. Y. Yuan, M. Zepf, and M. Borghesi, Phys. Rev. Lett. **109**, 185006 (2012).

[24] J. H. Bin, W. J. Ma, H. Y. Wang, M. J. V. Streeter, C. Kreuzer, D. Kiefer, M. Yeung, S. Cousens, P. S. Foster, B. Dromey, X. Q. Yan, R. Ramis, J. Meyer-ter-Vehn, M. Zepf, and J. Schreiber, Phys. Rev. Lett. **115**, 064801 (2015).

[25] F. Pegoraro and S. V. Bulanov, Phys. Rev. Lett. **99**, 065002 (2007).

[26] M. Chen, A. Pukhov, Z. M. Sheng, and X. Q. Yan, Phys. Plasmas **15**, 113103 (2008).

[27] M. Chen, A. Pukhov, T. P. Yu, and Z. M. Sheng, Phys. Rev. Lett. **103**, 024801 (2009).

[28] X. Q. Yan, H. C. Wu, Z. M. Sheng, J. E. Chen, and J. Meyer-ter-Vehn, Phys. Rev. Lett. **103**, 135001 (2009).

[29] X. Zhang, B. Shen, L. Ji, W. Wang, J. Xu, Y. Yu, and X. Wang, Phys. Plasmas **18**, 073101 (2011).

[30] B. Qiao, M. Zepf, M. Borghesi, B. Dromey, M. Geissler, A. Karmakar, and P. Gibbon, Phys. Rev. Lett. **105**, 155002 (2010).

[31] B. Qiao, M. Zepf, P. Gibbon, M. Borghesi, B. Dromey, S. Kar, J. Schreiber, and M. Geissler, Phys. Plasmas **18**, 043102 (2011).

[32] D. Wu, C. Y. Zheng, B. Qiao, C. T. Zhou, X. Q. Yan, M. Y. Yu, and X. T. He, Phys. Rev. E **90**, 023101 (2014).

[33] C. A. J. Palmer, J. Schreiber, S. R. Nagel, N. P. Dover, C. Bellei, F. N. Beg, S. Bott, R. J. Clarke, A. E. Dangor, S. M. Hassan, P. Hilz, D. Jung, S. Kneip, S. P. D. Mangles, K. L. Lancaster, A. Rehman, A. P. L. Robinson, C. Spindloe, J. Szerypo, M. Tatarakis, M. Yeung, M. Zepf, and Z. Najmudin, Phys. Rev. Lett. **108**, 225002 (2012).

[34] B. Eliasson, New J. Phys. **17**, 033026 (2015).

[35] A. Sgattoni, S. Sinigardi, L. Fedeli, F. Pegoraro, and A. Macchi, Phys. Rev. E **91**, 013106 (2015).

[36] B. F. Lasinski, A. B. Langdon, S. P. Hatchett, M. H. Key, and M. Tabak, Phys. Plasmas **6**, 2041 (1999).

[37] Y. Sentoku, K. Mima, S.-i. Kojima, and H. Ruhl, Phys. Plasmas **7**, 689 (2000).

[38] J. C. Adam, A. Héron, and G. Laval, Phys. Rev. Lett. **97**, 205006 (2006).

[39] A. Grassi, M. Grech, F. Amiranoff, A. Macchi, and C. Riconda, Phys. Rev. E **96**, 033204 (2017).

[40] Y. Wan, C. H. Pai, C. J. Zhang, F. Li, Y. P. Wu, J. F. Hua, W. Lu, Y. Q. Gu, L. O. Silva, C. Joshi, and W. B. Mori, Phys. Rev. Lett. **117**, 234801 (2016).

[41] V. P. Silin, Soviet Phys. Jetp-Ussr **21**, 1127 (1965).

[42] J. R. Sanmarti, Phys. Fluids **13**, 1533 (1970).

[43] F. Cattani, A. Kim, D. Anderson, and M. Lisak, Phys. Rev. E **62**, 1234 (2000).

[44] R. A. Fonseca, L. O. Silva, F. S. Tsung, V. K. Decyk, W. Lu, C. Ren, W. B. Mori, S. Deng, S. Lee, T. Katsouleas, and J. C. Adam, in *Proceedings of the Computational Science-Iccs 2002, Pt III*, Lecture Notes in Computer Science, edited by P. Sloot, C. J. K. Tan, J. J. Dongarra, and A. G. Hoekstra (Springer-Verlag, Berlin, 2002), pp. 342–351, Vol. 2331.